

Oxygen Vacancies in the Spotlight: On the Engineering of Intrinsic Defects in Highly Defective TiO₂ Photocatalysts

Daniela Meroni,^{1,2} Carolina Cionti¹, Lucia Silvestrini³, Noga Gal,⁴ Marco Cazzaniga,¹ Michele Ceotto,¹ Giacomo Buccella,⁵ Leonardo Lo Presti^{*,1,6} and Giuseppe Cappelletti^{1,2}

1. Università degli Studi di Milano, Dipartimento di Chimica, Via Golgi 19, 20133 Milano (Italy)
2. Consorzio INSTM, via Giusti 9, 50121 Florence (Italy)
3. Institute of Microbial Genetics, Department of Applied Genetics and Cell Biology, University of Natural Resources and Life Sciences (BOKU), Konrad Lorenz Straße 24, 3430 Tulln an der Donau (Austria)
4. Department of Bionosciences, University of Natural Resources and Life Sciences (BOKU), Muthgasse 11/II, 1190 Vienna (Austria)
5. Politecnico di Milano, Department of Chemistry, Materials and Chemical Engineering "Giulio Natta", Piazza Leonardo da Vinci 32, Milano (Italy)
6. Istituto Nazionale di Fisica Nucleare (INFN), Laboratori Nazionali di Frascati, Frascati (Italy)

* To whom correspondence should be addressed: leonardo.lopresti@unimi.it

ABSTRACT

Nanostructured oxide semiconductors are widely used in energy conversion, catalysis, sensing and environmental applications, due to their high stability, commercial availability, efficiency and low cost. Despite its crucial importance for the design of more efficient materials, the interplay between intrinsic and extrinsic defects is yet to be clarified. For example, oxygen vacancies (V_O 's) can be either beneficial or detrimental to the desired performances, depending on a variety of factors. Here, we synthesize TiO_{2-x} samples by the addition of three different N chemical sources (NH_3 , triethylamine, urea). X-ray absorption spectroscopy, confocal microscopy, UV-vis absorbance and fluorescence, are employed to explore the occurrence and location of V_O 's both in real and energy spaces. High-grade bulk DFT simulations complement the experimental picture. Synergy between theory and experiment, on the one hand, estimates the relative V_O 's content in the different samples from local structural information. On the other hand, a sharp optical transition at ≈ 2.7 eV serves an unequivocal spectral signature of V_O 's, allowing a semi-quantitative analysis by confocal microscopy. Fluorescence quenching of this feature is observed to a different degree in each sample under UV pumping and is attributed to the reaction of surface defects with atmospheric O_2 . Thus, we demonstrate that confocal microscopy can discriminate surface-localized V_O 's if coupled with the detection of O_2 -induced fluorescence quenching. Concurrently, UV-induced photochromism and visible light photodegradation shed light on the most effective reactive defects. Eventually, surface-localized oxygen vacancies are predominant where actual N substitutional doping occurs, leading to materials exhibiting visible-light activity and characteristic photochromic behaviour. Implications on strategies for concomitant V_O engineering and extrinsic doping are discussed.

1. INTRODUCTION

Oxide-based semiconductor materials are at the forefront of innovative technologies for pollutant remediation, renewable energy production and storage, optoelectronics, sensing and CO₂ reduction.¹⁻⁶ Being cheap, stable and highly versatile, as their properties can be tuned by adjusting the synthesis procedure⁷ and doping strategies⁸⁻¹⁰, oxide semiconductors are well-suited for large-scale industrial applications.

It is widely acknowledged that the intrinsic and extrinsic defectivity of semiconductor oxides plays a pivotal role in determining their physicochemical properties and ensuing performance. In particular, oxygen vacancies (V_O 's) are key players in determining the surface and bulk properties of semiconductor oxides, from adsorption behaviour to their electronic features.^{11,12} As a result, growing interest is being paid to strategies to control the V_O concentration and distribution.¹³⁻¹⁸ For instance, highly defective TiO_{2-x} materials have been extensively investigated to develop efficient photocatalysts, especially under visible-light irradiation. The most common synthesis protocols include thermal treatment with H₂,¹⁵ reduction with NaBH₄¹⁸ and doping with accurately chosen extrinsic species.¹⁷

Unfortunately, there is still an incomplete understanding on the interplay of different defects in determining the final material performance.¹² A case in point is represented by TiO_{2-x} materials, where V_O 's play a Jekyll-and-Hyde role. To ensure electroneutrality, V_O 's are accompanied by charged defects, like reducing Ti³⁺ centres.¹⁹ The latter are associated to shallow mid-gap states²⁰ that lower the apparent band gap and shift the main absorption edge into the visible region. Moreover, V_O 's increase the oxide adsorption properties, especially if they lie close to the oxide-solution interface.^{14,21} These merits clash against a faster electron-hole (e^-h^+) recombination,²² as the same V_O 's act as recombination centres that lower the lifetime of photogenerated e^-h^+ pairs. As a result, developing oxides with optimized performance is often a matter of trial and error.

The reasons for this lack of knowledge are twofold. First, techniques able to quantify the amount of V_O 's are not available, especially in the presence of dopants and/or multiphase systems. V_O 's are usually studied through X-ray photoelectron spectroscopy (XPS), X-ray absorption spectroscopy (XAS) and electron paramagnetic resonance (EPR) spectroscopy,²³⁻²⁵ which try to provide tentative quantifications but cannot easily discriminate among the various kinds of defects in complex matrices. Second, a further issue is the location of V_O 's defects, since bulk and surface species have different effects on adsorption and recombination phenomena.^{12,26} For instance, Cao et al. recently studied the influence of surface vacancies by transmission electron microscopy (TEM) and electron energy loss spectroscopy (EELS), in enhancing the photocatalytic activity of TiO₂ towards Rhodamine B degradation and hydrogen generation.²⁴ In any case, the occurrence of

significant amounts of bulk defects can be expected, especially at high dopant concentrations.²⁷ Doping by heteroatoms, such as N species, is thought to promote the formation of extra oxygen vacancies to ensure lattice electroneutrality. According to the Kröger–Vink notation, the equilibrium is:



That is, 1 mol of oxygen vacancies is needed to compensate 2 mol of substitutional nitrogen. However, the amount of defects is highly dependent also on the synthesis method, and particularly on the nitrogen precursor selected. It has been proposed that when ammonia or urea is adopted as N precursors during wet syntheses of TiO₂, the formation of labile NO-TiO₂ species²⁸ or of heterojunctions with *g*-C₃N₄²⁹ may preferentially occur instead of N-doping. In a recent review, Pulgarin and coauthors called for more studies to explore these issues.²⁸

This work aims to shed light on the interplay between oxygen vacancies and N species in TiO_{2-x} materials prepared using different N precursors (ammonia, triethylamine and urea). Their role on the optical, photochromic and photocatalytic properties of the resulting materials is discussed. Probes ranging from X-ray to UV-vis light, including X-ray absorption spectroscopy, confocal fluorescence microscopy, UV-vis absorption and fluorescence spectroscopy, are combined with high-grade DFT simulations to locate V_O centres both in the real and energy spaces. By this innovative approach, we disentangled the effects related to surface-localized V_O's defects in this complex, multi-defect systems.

2. MATERIALS AND METHODS

2.1 Synthesis of TiO₂ materials

All reactants were purchased from Sigma-Aldrich and used without further purification. Solutions and suspensions were prepared using doubly distilled water passed through a Milli-Q apparatus. Pristine and N-modified TiO₂ samples were synthesized by a sol-gel route using titanium (IV) isopropoxide (TTIP) as starting material and three different N-containing species (triethylamine, ammonia and urea) as N-sources. TTIP (30.7 mL) and 2-propanol (37.6 mL) were mixed in a 500 mL flask. Then, 180 mL of a basic solution containing KOH and a variable amount of N species was added dropwise while stirring at 300 rpm. The concentration of the basic solution was adjusted to fix the pH at 9. The adopted H₂O/TTIP and H₂O/2-propanol molar ratios were 100 and 20, respectively. The obtained gel was stirred for 90 min, then dried in oven at 80 °C overnight. Finally, the powder was calcined at 400 °C for 6 h under O₂ stream (9 NL h⁻¹).

Titania samples prepared with the addition of triethylamine (-T), urea (-U) and NH_3 (-N) are named “TNT_x”, “TNU_x” and “TNN_x”, respectively, with x standing for the nominal N/Ti molar ratio (x = 0.1 and 0.5), whereas the pristine one is labelled as “T”.

2.2 Materials characterization

Powder X-ray diffraction (PXRD) patterns were collected using graphite-monochromated Cu $K\alpha$ radiation on a Philips PW 3710 Bragg-Brentano goniometer equipped with a scintillation counter and 1° divergence slit, 0.2 mm receiving slit and 0.04° Soller slit systems. Scans were recorded at 40 kV x 40 mA nominal X-rays power between 20° and 90° , using a step size 0.1° wide. Instrumental line broadening effects were corrected using a microcrystalline Si-powdered standard. The average crystallite size for the anatase phase was determined applying the Scherrer equation to the (101) most intense non-overlapping reflection attributed to this phase.

The specific surface area of the samples was characterized by adsorption-desorption isotherm of N_2 in subcritical conditions using the Brunauer–Emmett–Teller (BET) method on a Coulter SA3100 apparatus. Total pore volume was determined from desorption isotherms using the Barrett-Joyner-Halenda (BJH) method.

Diffuse reflectance spectroscopy (DRS) measurements were carried out on a Shimadzu UV-2600 UV-vis spectrophotometer, equipped with an integrating sphere. Spectral scans were performed in the 250-700 nm range, using BaSO_4 as a reference. Apparent band gap values, E_g , were determined according to the Kubelka-Munk method.³⁰ Spectral measurements were carried out before and after irradiation with UV, using a Jelosil HG500 halogen lamp with an effective power density of 17.0 mW cm^{-2} between 280 and 400 nm. To ensure the reproducibility of the measurements and avoid inhomogeneous irradiation of the powder samples due to light penetration effects, the DRS sample holder was packed with a proper amount of ground and homogenized powder to prepare a compact, flat and homogeneous surface. The sample was then analyzed with the spectrophotometer, irradiated without removing it from the sample holder and remeasured at set time intervals.

Extended X-ray absorption fine structure (EXAFS) spectra were recorded at the Swiss-Norwegian beamline (BM01B) at the European Synchrotron Radiation Facility (ESRF). The TiO_2 powder was diluted in CaCO_3 to avoid thickness effects. X-ray absorption curves were collected in transmission mode across the Ti K-edge at room temperature. A Si (111)-monochromated beam was employed, either in the 4.9–5.4 keV (pure TiO_2) or in the 4.9–5.8 keV (TNN, TNU and TNT series) energy ranges. The Horae suite of programs,³¹ based on the IFEFFIT library,³² was used throughout for data processing and fitting, adopting the same strategy described in detail elsewhere.²⁷ Section S1 in the Supporting Information summarizes the details of the least-squares fittings.

UV-Vis fluorescence spectra were recorded with a LS55 fluorescence spectrophotometer on water-suspended nanostructured TiO₂ powders. Two scan modes were employed. In the “excitation” (EX) one, the spectral intensity was monitored as a function of the pumping wavelength, looking at a fixed fluorescence emission of 2.254 eV ($\lambda = 550$ nm). In the “emission” (EM) mode, the excitation wavelength was fixed at 3.179 eV ($\lambda = 390$ nm), which corresponds to the maximum of the EX scan. Then, the fluorescence intensity was probed as a function of the emitted wavelength. Raw spectral data were normalized according with the procedure proposed by Angulo and co-workers.³³

Images of TNN, TNU and TNT samples were acquired by confocal laser scanning microscope (CLSM) Olympus FV1000. A spot of 1000x diluted TiO₂ nanoparticles, previously vortexed and heated, was aliquoted on a microscopy glass. More in detail, an aliquot of the water-suspended nanoparticles stock (1:1 v/v) was diluted in distilled water in order to observe an appreciable decrement of nanoparticle aggregates. The best resulting dilution of the nanoparticles stocks was 1000x. Then, 5 μ L were put on a laboratory slide and analyzed. Great care was taken to optimize the operational parameters of the laser and the detector. Excitation was performed at the lowest wavelength achieved by the microscope (405 nm). The detector voltage was initially set at 580 V, which allowed us to consider luminescence of pristine TiO₂ nanoparticles close to zero, the calibration state for the quantification of emission related to N addition. As indicated below, the detector voltage was incremented to 700 V, due to the unexpected background luminescence of pristine TiO₂ nanoparticles which could be due to intrinsic material defects. This increment enables to detect the minimal luminescence of particles by keeping a low laser intensity (10%). When the laser intensity was increased to 12.9%, the fluorescent spots could be clearly appreciated (Figures S10–S12), but without an accurate determination of the intensities, as the photon flux overcame the linearity interval of the detector. A lower laser intensity, coupled with a lower sample loading, was deemed necessary to quantify the fluorescence intensity by microdensitometry. The microscope ouerture was set at 4x and the offset values within the range of 30-50%. Particles detected on each image were counted by Image J Fiji software³⁴ and the related luminescence intensity was calculated.

Confocal microscopy is sensitive to the distribution of active fluorophores within the bulk volume of each independent crystal lattice. However, in the present case, samples are aggregates of nanostructured particles (Figures S10–S12), which have μ m-to-mm large thickness and can shield the fluorescence output effectively. Moreover, both total integrated intensity and self-absorption depend on the amount of material in the active eyepiece area. To provide quantitative estimates, as well as reliable comparisons among different materials, we define a fluorescence density output, I_D as:

$$I_D = \frac{I_f}{A_{lum}} \quad (3)$$

and a total specific fluorescence, I_S according to:

$$I_S = \frac{I_f}{A_{tot}} \quad (4)$$

where I_f is the total integrated fluorescence intensity (in arbitrary units) as retrieved from the visible blue spots of each image, A_{lum} is the corresponding total emitting area and A_{tot} the total area covered by nanoparticle aggregates (in μm^2). I_D represents the average emitting density per unit area. It is easy to see that the I_S/I_D ratio corresponds to the A_{lum}/A_{tot} ratio, that is, to the relative amount of emitting area with respect to the total area. As extrinsic and intrinsic defects are expected to be distributed randomly through each whole nanostructured powder, we propose to take the quantity $\omega = 1 - A_{lum}/A_{tot} = 1 - I_S/I_D$ as a measure of the self-absorption due to aggregation of the nanoparticles.

2.3 Photocatalytic tests

The photocatalytic activity of the samples was tested towards the gas phase degradation of a model volatile organic compound (ethanol) under either UV (Jelosil HG500 halogen lamp) or visible light (Lot Oriel halogen lamp equipped with a 400 nm long wave pass edge filter). Effective power density values during photocatalytic tests were determined using a Thorlabs S314C radiometer and were 17.0 and 2.4 mW cm^{-2} for UV and visible light irradiation, respectively. The adopted photocatalytic apparatus was described previously³⁵ and allows monitoring via a gas-chromatographic system (Agilent 7890 equipped with Porapak and DB-VAX columns, a methanator and two FID detectors) both ethanol disappearance, intermediate formation (acetaldehyde) and build-up of CO_2 as mineralization final product. The TiO_2 powders were drop casted on a Petri dish: 50 and 70 mg of sample powder, corresponding to an irradiated area of 51 and 102 cm^2 , were used respectively for UV and visible tests due to the different reaction rates provided by the two irradiation sources. An ethanol starting concentration of 238 ppm was employed for all tests.

2.4 DFT simulations

Theoretical simulation were performed with the ab initio plane-wave Quantum-Espresso (Q-E) suite^{36–38} with a PBE+U level of theory. For the Hubbard U we choose a value of 3.5 eV since it provides a compromise between the increasing band gap and preserving lattice parameters comparable with experiment.^{39,40} The core electrons are accounted by ultrasoft pseudopotentials and we set the energy cutoff to 50 Ry for the wavefunctions and 400 Ry for the electron density. We obtained the theoretical lattice parameters of anatase by performing a variable cell optimisation with a $10 \times 10 \times 10$ k-points mesh obtaining a lattice parameter $a=3.838 \text{ \AA}$ and $c=9.711 \text{ \AA}$ (reasonably close

to the experimental values of $a=3.782 \text{ \AA}$ and $c=9.502 \text{ \AA}$)⁴¹ with an electronic band gap of 2.477 eV (still smaller than the experimental value of 3.2 eV).⁴¹ The supercell has been generated by $3 \times 3 \times 1$ replicas of the conventional cell and, consequently, the k-points sampling was reduced to a $2 \times 2 \times 2$ mesh for the supercell. Since the removal of an oxygen atom in the supercell yields to a pair of excess electrons, all the calculations have been performed with a collinear spin polarization (unrestricted DFT) with the orbital occupation described adopting a gaussian smearing of 0.005 Ry. We tested several starting guesses, eventually identifying the most stable spin configurations (both with parallel and antiparallel spins). We found a substantial agreement with previously published results.^{19,42–47} For the detected states we analyzed the Spin Density, total Density of States (DOS), its Projection on selected atoms (PDOS), and computed the Bader charges. To achieve reliable results for the DOS we increased the k -point sampling adopting a $5 \times 5 \times 5$ mesh. Finally, the Bader analysis have been performed thanks to the Critic2 code^{48,49} starting from the electron density obtained from the Q-E code.

3. RESULTS

3.1 Structural and optical properties

Table 1 reports the main physicochemical properties of the prepared samples: in all cases, anatase-brookite composites were obtained, with N addition favouring a higher anatase content, in agreement with previous reports.⁷ The addition of ammonia also promotes the sample crystallinity, almost doubling the anatase crystallite size.⁷ Upon N addition, samples exhibit a lower surface area and porosity compared to the pristine reference, especially in the case of urea addition, fully in accordance with the literature.⁵⁰

Moreover, N addition also induces a visible light absorption in all tested samples,^{27,50} although the optical properties vary with the type of N source adopted, as shown by Figure 1. Ammonia and urea give rise to a localized absorption centred around 2.65 eV, with no appreciable shift in the absorption edge (as shown by the derivative graph, Figure 1, inset). As a result, the apparent band gap value is hardly modified with respect to the pristine reference (Table 1). Increasing the urea content promotes the visible light absorption, whereas no changes are observed in the case of ammonia, probably because of the high volatility of NH_3 (during the calcination step) which may limit the effective amount of N species introduced.

Visible light sensitization upon urea addition has been attributed to the formation of $g\text{-C}_3\text{N}_4$ during calcination at temperatures $> 350 \text{ }^\circ\text{C}$.²⁹ According to the literature,⁵¹ it is known that $g\text{-C}_3\text{N}_4$ gives rise to intense bands in the $1200\text{-}1600 \text{ cm}^{-1}$ region, in particular, bands at 1250, 1330, 1400, and 1530 cm^{-1} related to the stretching vibration mode of CN heterocycles.

Table 1. Physicochemical characteristics of the synthesized TiO₂ samples (phase composition: A for anatase, B for brookite; average anatase crystallite size, $d_a^{(101)}$; specific surface area, S_{BET} ; total pore volume, V_{pores} ; apparent band gap value, E_g) and their photocatalytic performance during UV and visible tests in terms of pseudo-first order kinetic rate constant of ethanol degradation, k , and %CO₂ evolved after 30 min of reaction.

sample	phase composition %	$d_a^{(101)}$ (nm)	S_{BET} (m ² g ⁻¹)	V_{pores} (mL g ⁻¹)	E_g (eV)	photocatalytic tests		
						$k_{EtOH,UV}$ (x10 ³ s ⁻¹)	%CO _{2,UV} (30min)	$k_{EtOH,vis}$ (x10 ⁴ s ⁻¹)
T	A: 73 B: 27	6	173	0.240	3.23	70±2	84.7	1.6 ± 0.4
TNN 0.1	A: 85 B: 15	11	112	0.152	3.23	69±2	77.1	1.7 ± 0.4
TNN 0.5	A: 95 B: 5	14	113	0.163	3.23	99±5	94.7	3.9 ± 0.2
TNU 0.1	A: 84 B: 16	9	70	0.071	3.18	66±1	51.6	3.1 ± 0.3
TNU 0.5	A: 88 B: 12	9	53	0.090	3.20	56±1	14.2	1.4 ± 0.4
TNT 0.1	A: 85 B: 15	8	154	0.191	3.06	70±3	74.5	13.8 ± 0.6
TNT 0.5	A: 90 B: 10	9	100	0.029	3.00	54±1	14.4	6.4 ± 0.6

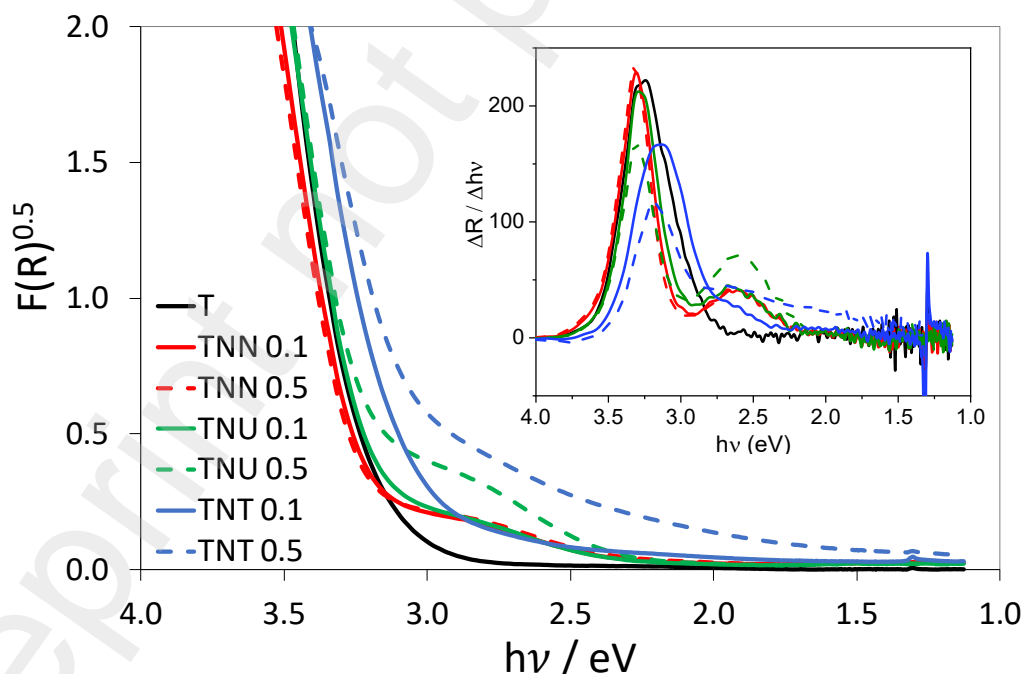


Figure 1 – Kubelka-Munk graph as a function of light energy for the synthesized TiO₂ samples. Inset: Relative first derivative of DR spectra.

In the present case, however, TNU samples do not exhibit any additional IR features in the 1200-1600 cm^{-1} region compared to the pristine TiO_2 sample, even at the highest tested urea content (Figure S1). This observation is consistent also with photocatalytic data (see Section 3.6).

The addition of triethylamine provokes instead a red-shifted absorption edge, lowering the apparent band gap (Table 1). Furthermore, TNT samples present also a broad absorption in the visible range, more clearly appreciable in the TNT0.5 sample (Figure 1).

3.2 Local structure

The local structure of the synthesized materials was investigated by EXAFS spectroscopy, which is sensible to the average short-range structure of the probed absorbing atom, particularly to the first coordination shell. In the present case, any distortion from the expected crystallographic anatase structure, which is based on axially elongated TiO_6 octahedra, can be attributed to synthesis-induced lattice defects (Table 2). Owing to the nanometer-size distribution of the samples, we focused just on point defects, which imply substitutional N (N_O), interstitial N (N_i) and oxygen vacancies (V_O). We relied upon periodic quantum simulations to disentangle the different structural effects triggered by the various defects, according to a previously reported approach²⁷. While N_O 's leave unchanged the average Ti–O coordination distances, N_i 's lengthen them by up to 5-6%. The reason is that the Ti site symmetry is poorly perturbed by a N_O defect, while N_i produces η^2 coordinated N=O species that strongly distort the local Ti environment. On the contrary, V_O 's determine an apparent $\approx 3\%$ shrinkage of the average Ti–O distances. In all cases, the longest axial bonds are the most affected Ti–O distances. Keeping in mind these scenarios, Table 2 reports the average Ti–O first coordination distances as a function of the nominal N/Ti content.

Table 2. Average axial and equatorial Ti–O distances as a function of the nominal N/Ti ratio, as estimated from the least squares against EXAFS data on TiO_2 samples. Results for the TNT series are the same already reported in ref.⁵². Estimated standard deviations (e.s.d.'s) in parentheses. See Section S1 for details of the least-squares fittings.

<i>N/Ti nominal ratio</i>	<i>axial</i>			<i>equatorial</i>		
0	2.04(2)			1.82(1)		
	<i>TNT</i>	<i>TNN</i>	<i>TNU</i>	<i>TNT</i>	<i>TNN</i>	<i>TNU</i>
0.1	2.04(2)	2.05(5)	2.08(5)	1.81(1)	1.84(2)	1.80(2)
0.5	1.93(3)	2.07(5)	2.06(6)	1.83(1)	1.85(2)	1.83(3)

The average equatorial distances are reasonably close to the crystallographic reference⁵³ and remain unchanged at increasing N precursor amounts. In contrast, the trend of axial distances depends on the N chemical source. At high N concentrations, TNT samples present a significant amount of

oxygen vacancies,²⁷ as it can be appreciated by the apparent reduction of the average Ti–O bond length. This is not the case for urea and ammonia, where axial Ti–O distances remain equal to the pristine reference within 1 estimated standard deviation. Thus, no patent distortions are detectable in the average local TiO₆ structure. This implies that the urea- and ammonia-derived materials do not bear any marked V_O excess compared to the pristine TiO₂.

3.3 Photochromism

The photochromic properties of TiO₂ samples were studied to investigate the nature of light-active trap centres in the three series of samples. Photochromism is normally interpreted in terms of light-induced formation of charge carriers, followed by their separation at electron and hole traps, thermally-stimulated detrapping and recombination.⁵⁴

Figure 2 reports differential spectra of the synthesized samples, obtained as difference between the reflectance (*R*) curves of the same sample before and after irradiation with broadband UV light.

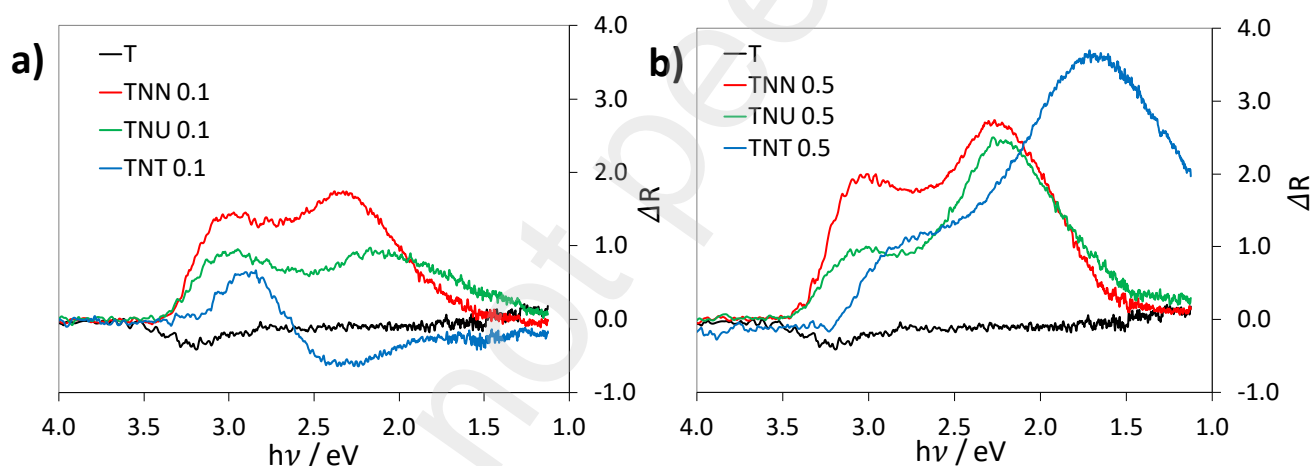


Figure 2 – Effect of UV irradiation, as variation in reflectance, on the optical properties of synthesized samples with N/Ti nominal ratio of 0.1 (a) and 0.5 (b). The relative spectrum of the pristine TiO₂ reference is reported for the sake of comparison.

Following Serpone and coworkers,⁵⁵ the transmittance of titania samples can be safely assumed to be zero, being them opaque to visible light. In Figure 2, a positive peak means an increase in absorbance (*A*) upon treatment with UV light, whereas a negative peak implies a corresponding decrease in absorbance. We denote with the as *R*₀ and *R*_{irr} the reflectance respectively before and after the UV irradiation process. Then, $R + A = 1$ and $\Delta R = R_0 - R_{irr} = (1 - A_0) - (1 - A_{irr}) = A_{irr} - A_0$. If $\Delta R > 0$, it follows that $A_{irr} > A_0$, that is, the irradiated sample absorbs more than the not-irradiated one. An increase in light absorption upon UV irradiation is appreciable for most of the samples, especially at

the highest N/Ti ratio. This suggests that the number of absorbing defects is growing, whereas a decrease in absorbance implies photobleaching.⁵¹ The pristine sample T shows no change in light absorption after UV irradiation. This implies that photochromism is not due to the intrinsic electronic properties of TiO₂.

A fitting of the differential spectra was performed using Gaussian curves⁵⁶ and peak positions, along with peak width and relative area, are reported in Table 3. Details of the fitting procedures and deconvoluted spectra are reported in the Supporting Information (Figure S3).

Table 3. Least-squares fitting of differential DRS features reported in Figure 2.

Sample	peak 1			peak 2			peak 3		
	position <i>n</i> (eV)	width (eV)	area %	position (eV)	width (eV)	area %	position (eV)	width (eV)	area %
TNN0.1	3.00	0.39	30	2.32	0.67	70	-	-	-
TNN0.5	3.03	0.39	27	2.27	0.69	73	-	-	-
TNU0.1	2.97	0.45	36	2.10	0.75	64	-	-	-
TNU0.5	3.05	0.31	12	2.21	0.78	88	-	-	-
TNT0.1	2.88	0.30	35	2.30	0.49	44	1.51	0.64	21
TNT0.5	2.65	0.52	15	2.03	0.58	25	1.49	0.75	60

Also in this case, the TNN and TNU samples exhibit similar behaviour, showing two main components at around 3.0 and 2.2 eV (the latter being the most intense), which imply an improved absorption in the violet (430 nm) and green (530 nm) regions. Conversely, TNT samples show a more complex behaviour. Besides a positive component at ca. 2.9 eV, TNT0.1 is the only specimen that shows a patent broad decrease in absorbance in the 1.8-2.6 eV range (Figure 2a), *i.e.* in the 690–480 nm (red-blue) region of the visible window, with the minimum lying at 2.3 eV (539 nm). This feature indicates that only UV irradiation reduces the amount of trapped electrons for TNT0.1. On the other hand, TNT0.5 presents all positive peaks, with main components at ca. 2.0 and 1.5 eV (Figure 2b).

Overall, these data suggest a similar nature and content of trap defects in TNN and TNU samples, supporting also a lesser role of the nominal N/Ti ratio on the former. Moreover, in good agreement with EXAFS data, photochromic spectra show the presence of additional trap defects for the TNT series and a far higher defectivity for TNT0.5 compared to TNT0.1.

3.4 Photoluminescence

The photophysical properties of the samples were investigated by UV-vis fluorescence spectra, as reported in Figure 3.

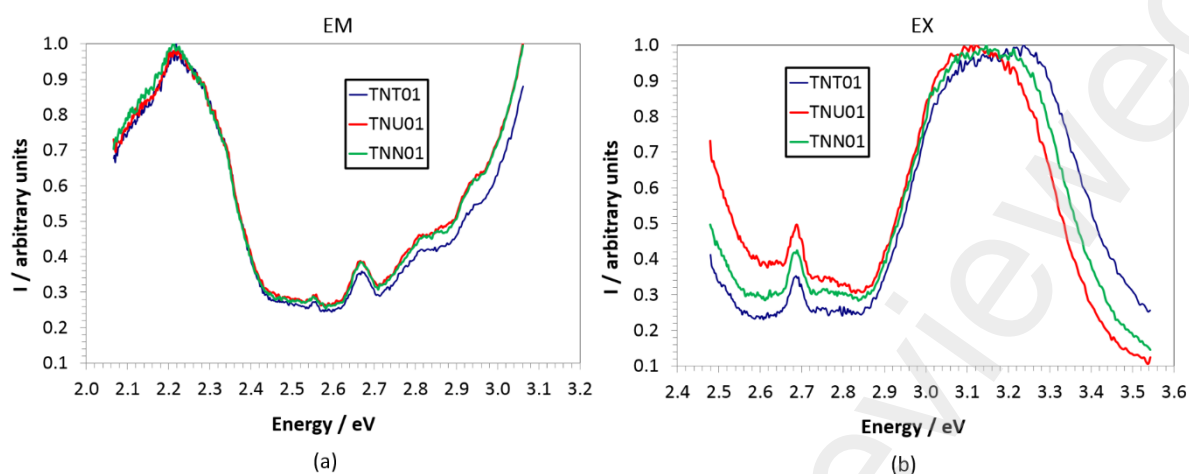


Figure 3. Normalized³³ emission (“EM”) (a) and excitation (“EX”) UV–Vis fluorescence spectra for synthesized TiO₂ samples from different N sources (blue: triethylamine, red: urea, green: ammonia) with nominal N/Ti ratio of 0.1. Other concentrations are shown in Figure S4.

Two almost symmetrical curves are shown for each specimen, referring to the same electronic transitions, followed through excitation (“EX” spectra) or emission (“EM” spectra). The horizontal distance between the main symmetrical features quantifies the corresponding Stokes shifts. In excitation mode (Figure 3b), the most intense band starts at roughly 2.9 eV and shows a broad maximum around 3.1–3.2 eV (395–397 nm), which corresponds to the adiabatic (vertical) transition across the anatase band gap. Owing to the indirect nature of this semiconductor, dissipative processes involving lattice phonons downshift the emission by ≈ 0.9 – 1.0 eV through non-radiative decay, resulting in a maximum close to 2.2 eV (Figure 3a).

Three points are worth noting. First, all the spectra bear the same peak at ≈ 2.68 eV (461–464 nm), which undergoes an almost negligible Stokes shift of ≈ 0.017 eV. This feature is not attributable to N species, as it is already detectable in the pristine specimen T (Figure 3).

Second, the signal of the TNN and TNU series closely resembles that of the blank reference (see Figure S4 SI), with root mean square deviations invariably lower than 0.025 (TNN) or 0.020 (TNU) normalized intensity units between the corresponding curves. Moreover, signals corresponding to 0.1 and 0.5 N/Ti nominal ratios are almost completely superimposable in both the TNN and TNU series, as it can be appreciated by visual inspection of Figure 3. In other words, when the precursor is either urea or ammonia, the nominal N concentration does neither significantly affect the band edges, nor it is expected to strongly reduce the band gap. This agrees with the DRS results shown in Table 1 and Figure 1.

The picture changes when the TNT series is considered (Figure 3). A ≈ 0.11 eV large downshift of the maximum of the main absorption band is apparent at higher N concentration in the excitation scan mode. This is comparable with the decrease in the apparent band gap (0.1-0.2 eV) detected by DRS measurements (see Section 3.1). The shape of the high-energy excitation band is also influenced. As the shift does not affect the emission signal, we must conclude that non-radiative decay mechanisms reset the differences among distinct excitation paths, as the radiative step of the relaxation process starts from the energy of the absolute conduction band minimum (CBM) and results to a 2.1-2.2 eV wide step. On average, TNT spectra are significantly more different compared to the pristine reference, with root mean square deviations of ≈ 0.040 normalized intensity units. This further confirms that the electronic properties of TiO₂ are significantly affected only when the material comes from the triethylamine precursor, in accordance with DRS analyses (see Section 3.1).

3.5 Periodic DFT results

To clarify the relationship between defectivity and photophysical features, we exploited DFT to simulate an anatase TiO₂ supercell with a single V_O. The purpose was to disclose the genuine electronic and structural effects of V_O, getting rid of possible interactions with extrinsic dopants.^{20,50} In particular, we look for the possible occurrence of colour centres and changes affecting the formal oxidation state of Ti ions. An oxygen vacancy implies that two excess electrons must be accounted for to ensure electroneutrality of the lattice. Within our PBE+U approach (U=3.5 eV), among the possible stationary states we identified seven possible electronic states, differing in either the spin pairing or the relative localization of the excess electrons. A full description, as well as a discussion on the relative stability of the different states, is reported in Section S4. We consider the least stable nonmagnetic closed shell state as a suitable reference for the subsequent discussion. The six magnetic solutions all have lower energies. The magnetization yields to a total energy reduction with the most stable state presenting an energy -0.51 eV below the unpolarized case, implying a high localization of the excess electrons on different Ti atoms, one adjacent to the V_O and the other slightly further (Figure 4a).

Two almost degenerate spin configurations are possible for this state, the one with parallel spins being more stable of the order of 10^{-3} eV. The -0.51 eV stabilization comes from the relief of unshielded Coulomb repulsion, which requires the excess electrons being localized into sites far apart from each other. At the same time, it is reasonable that electrons on different metal ions show a poor spin correlation in a diamagnetic matrix. Moreover, our ground-state simulations do not predict the formation of Farbe centres in the V_O void.

A closer insight can be achieved by inspecting the net charges of atoms involved in the internal reduction $\text{Ti}^{4+} + e^- \rightarrow \text{Ti}^{3+}$. We evaluated integral atomic charges from the topological analysis of the total charge density, according to the Bader's Quantum Theory of Atoms in Molecules (QTAIM);⁵⁷ full results are shown in Tables S4-S5. Granted that individual charges are not quantum observables, and henceforth any partitioning scheme is arbitrary to say the least, the QTAIM approach has the advantage of subdividing the total charge density into non-overlapping disjoint regions ("topological atoms", Ω 's), whose boundaries are self-consistently set by the topology of the $\nabla\rho(\mathbf{r})$ vector field. Thus, the net charge of each topological atom is defined as:

$$q(\Omega) = Z_{\Omega} - e \cdot \int_{\Omega} \rho(r) dr \quad (2)$$

where Z_{Ω} is the positive charge of the nucleus in Ω and e is the elementary charge. QTAIM charges $q(\Omega)$ depend on the electron population of the topological basin Ω , which can be taken as a reliable estimator of the oxidation state of that atom in its crystalline environment.^{58,59} As for the present case, QTAIM charges confirm that the excess electrons are localized on specific Ti ions close to the V_{O} defect (Table S4), which bear $\approx 15\%$ more electrons than the corresponding bulk Ti atoms.

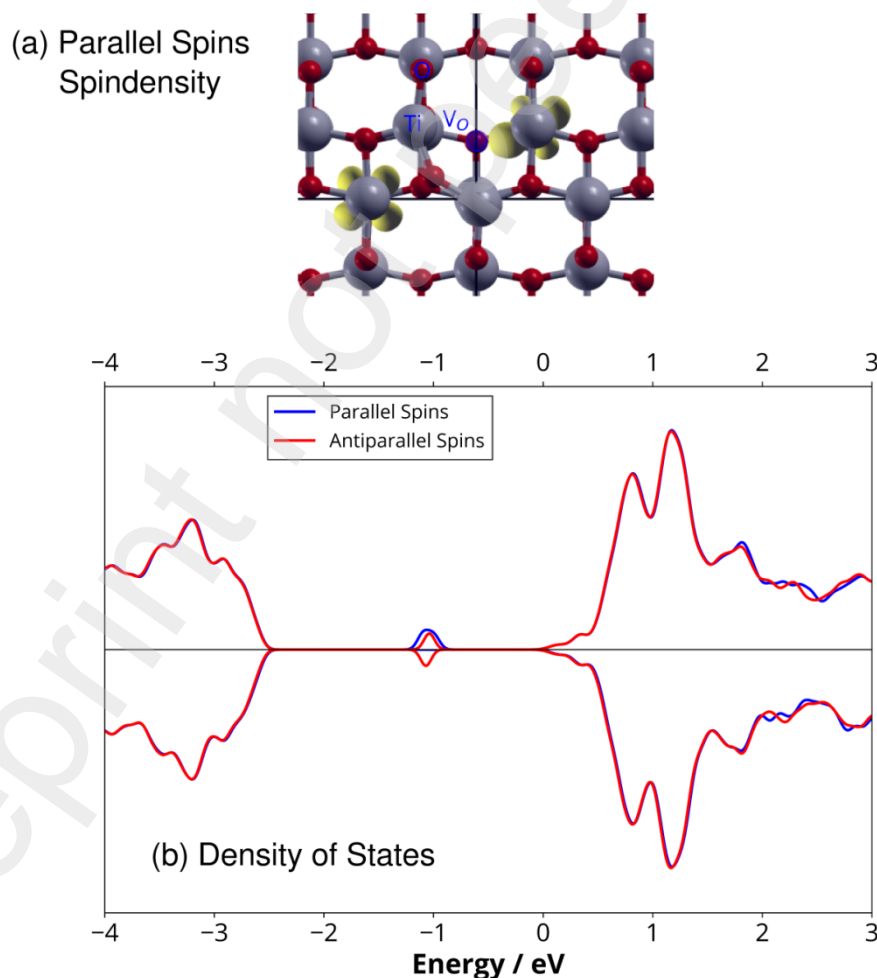


Figure 4. a) Spin density isolevel (yellow) at $5 \cdot 10^{-3}$ atomic units of the most stable state in oxygen-defective anatase TiO_2 with the PBE+U exchange and correlation potential. Ti atoms: grey. O atoms: red. The blue circle highlights the position of the oxygen vacancy. b) Density of States of defective anatase TiO_2 with the PBE+U exchange and correlation potential. Comparison of different magnetization states for the bulk and defective system. Upper and lower panels are for the two different unrestricted spin magnetization.

We note that the oxygen vacancy is equatorial with respect to both the reduced Ti centres (Figure 4a). An analogous behaviour is observed for all the magnetic solutions (Table S4-S5), with some V_{O} -neighbouring Ti atoms being reduced to some extent. Considering the band structure, the excess electrons inject new electronic states inside the band gap with respect to perfect TiO_2 (see Table S3 and Figure 4b). It is clear from the above discussion that these must be localized on Ti centres close to the V_{O} , as it can be appreciated also from the projected density of state (PDOS) schemes (Figure S8). Moreover, they fall deep inside the band gap, with a minimum distance from the conduction band minimum (CBM) of 0.9–1.0 eV for the two most stable solutions, as supported by a recent combined theoretical and experimental approach.²⁶ When related to the total DFT-predicted magnitude of the indirect band gap (2.48 eV), they correspond to ≈ 36 -40% of the latter (Figure 4b). Remarkably, this is in quantitative agreement with the UV-vis fluorescence results discussed in Section 3.4, where excitation and emission spectra show a signal at 1.06 eV from the indirect-gap CBM. Moreover, the highly localized nature of the defect complies well with the immaterial Stokes shift measured for the corresponding transition (see Section 3.4), indicating that the relaxation process is essentially radiative in nature. This is expected, considering that bulk V_{O} 's can act as efficient recombination centres. Hence, bulk DFT calculations support an attribution of the spectral feature noted in UV-Vis fluorescence experiments at 2.68 eV to oxygen vacancies, in agreement with previous reports.⁶⁰

3.6 Confocal Microscopy

As the aforementioned transition falls in the blue region of the visible window (461-464 nm), confocal microscopy (CM) can be employed to quantify the relative amount of fluorescence attributable to emitting V_{O} centres in our samples. CM is an imaging technique that allows locating fluorophores with high spatial resolution ($<0.5 \mu\text{m}$), even in complex matrices.⁶¹ In the present case, the specimen is a suspension of nanoparticle aggregates (Figure 5), hence data processing was performed taking into account the issue of self-absorption (see Section 2.2).

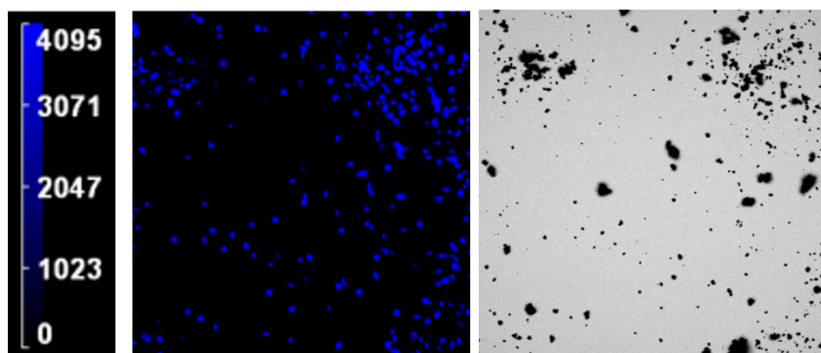


Figure 5. Confocal images (40x, area: 310 x 310 μm^2 , offset correction 50%, HV 700V, laser intensity 10%) of TNN0.5. Left: fluorescence in false colors to enhance the fluorescence output. Legend in arbitrary units. Right: visible light. This picture has an illustrative purpose to see what information the confocal images convey; see Figures S10-12 to see all samples.

In particular, I_D quantifies the average emitting density of regions whose fluorescence is not hampered by aggregation effects. Thus, I_D is uncorrelated with self-absorption (Figure S13) and it can be taken as a least-biased intrinsic property of the material, genuinely related with the nature of V_O defects. Figure 6 shows I_D estimates for the three series. Results are also summarized in Table S6.

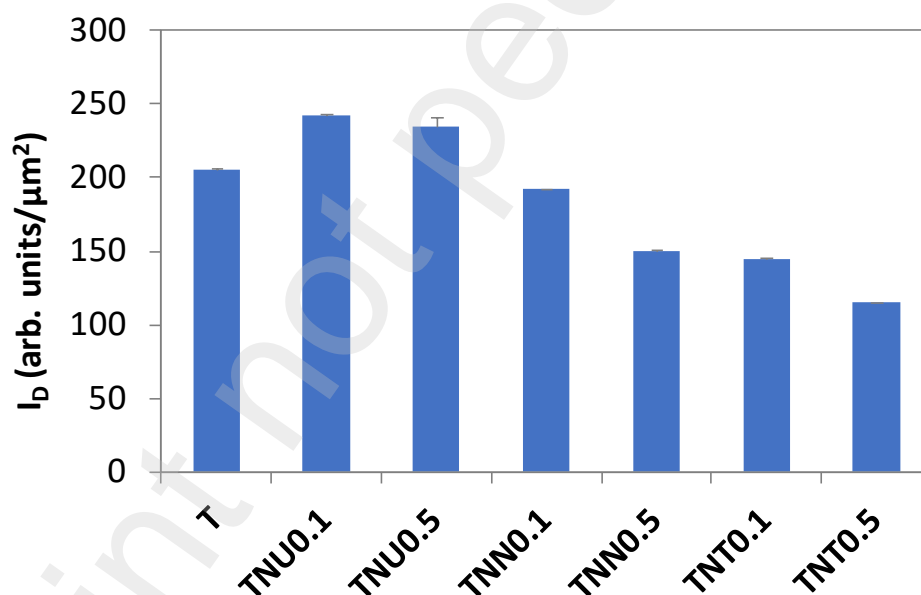


Figure 6. Fluorescence density (in arbitrary units per μm^2) of the synthesized samples, as estimated by confocal microscopy.

A first outcome from Figure 6 is that TNT materials have the lowest fluorescence output: their I_D is almost halved with respect to T, despite of a similar self-absorption (Table S6). This is quite surprising, as EXAFS results (Table 2) neatly demonstrate that the TNT series displays a promoted formation of extra oxygen vacancies. The latter can be attributed to an effective incorporation of extrinsic N defects in the lattice in the TNT series, according to Eq. 1. Furthermore, the trend shown

in Figure 6 countercorrelates with the expected amount of N that enters the lattice, as inferred from the distortion of the crystallographic unit cell of TiO₂ anatase (TNT > TNN > TNU) described elsewhere⁷. It should be noted that Figure 6 compares the fluorescence emission from V_O centres, *i.e.* the amount of radiative recombination from these species, and not the actual density of oxygen vacancies. The discrepancy between EXAFS and CM outcomes entails that V_O centres with different de-excitation pathways exist in each series, as will be further discussed in Section 4.

3.7 Photocatalysis

The role played by these different defective ensembles on the photocatalytic performance of the material was investigated towards the degradation of a model volatile organic compound, ethanol, in the gas phase (Figures S14-S15). Under UV light irradiation, pristine TiO₂ performs better than most of the visible-sensitized samples, both in terms of ethanol disappearance and of final mineralization (Table 1). This result could be rationalized considering the much lower specific surface area of N-modified samples with respect to the pristine reference. It is well-known that the morphological features of the photocatalyst play a major role on gas phase reactions: in the gas phase photocatalysis, only the adsorbed pollutant molecules can undergo redox reactions by photogenerated charge carriers or surface radicals.⁶² Moreover, the occurrence of lattice defects has been related to poorer photocatalytic performance by promoting recombination⁶³ or lowering the oxidative potential of photogenerated charges.²⁸ Notably, the only exception is represented by TNN0.5, which showed promoted photocatalytic performance, despite the lower surface area. The enhanced performance could be possibly related to the higher anatase content and crystallinity.

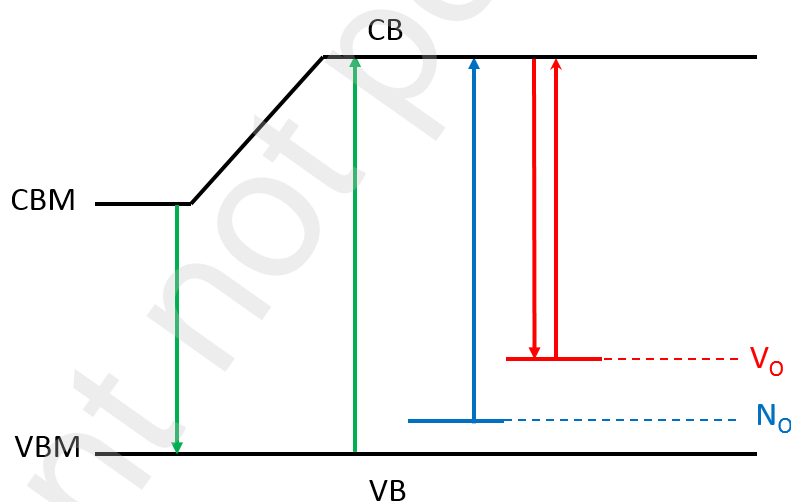
The role of N-addition on the photocatalytic performance under visible light irradiation was also investigated. Overall, the reaction rates are much lower than under UV irradiation, as a result only the rate constant of ethanol degradation are here commented (Table 1). Interestingly, most of the visible-sensitized samples do not exhibit significantly enhanced performance compared to the pristine reference. The residual activity of the latter under visible irradiation is due to the light absorbance above 400 nm of anatase. The best performing samples belong to the TNT series, with the TNT0.1 showing a reaction rate under visible light one order of magnitude higher than that of pristine TiO₂.

4. DISCUSSION

The reported experimental evidence underlines a diverse role of the three N sources in introducing intrinsic and extrinsic defects into the oxide lattice. Upon triethylamine addition in synthesis, the local structure and photophysical properties, in agreement with previous PXRD

studies,⁷ support N substitution of O atoms within the TiO₂ lattice, leading at high N nominal contents to a marked increase in the amount of V_O, in accordance with theoretical calculations.⁶⁴ Conversely, the TNN and TNU samples exhibit a localized visible-light absorption but miss the tell-tale signs of N substitutional doping (shift of the absorption edge and promotion of oxygen vacancies formation⁶⁴), in accordance with previous reports of TiO₂ modification using either ammonia or urea.²⁸ However, the nature of visible-light inducing defects in these samples remains controversial. Promoted PL emission from the TNU series suggests a fast charge carrier recombination, possibly explaining the observed poor photocatalytic performance of these samples (Section 3.7). These observations also do not support the formation of efficient TiO₂/g-C₃N₄ heterojunctions in the present conditions, as also suggested by FTIR spectra (Section 3.1). Furthermore, the similar photophysical behaviour of TNN and TNU samples seems to underscore common traits related to trap sites (see e.g., photochromic and PL properties).

Samples from different N sources thus present notable differences in terms of V_O's density. CM results suggest that each series differs also in the de-excitation pathways available for V_O centres. Scheme 1 summarizes the mechanisms of photoexcitation and relaxation of defective TiO₂ here proposed on the grounds of the present spectroscopic analyses, theoretical calculations and literature results²⁰.



Scheme 1. Qualitative illustration of the main radiative excitation-relaxation processes in TiO₂-based nanoparticles discussed in this work. CBM and VBM are the conduction band minimum and the valence band maximum. Green: main absorption path, already active in bare anatase TiO₂. The difference in energy between CB and CBM corresponds to the Stokes shift seen in UV-vis fluorescence spectra and involves a phonon-mediated non-radiative decay. Blue: absorption from occupied shallow mid-gap states due to substitutional N (estimated from bulk plane-wave calculations²⁰). Red: radiative excitation-relaxation process due to oxygen vacancies, with no significant Stokes shift (UV-vis fluorescence data, this work).

In this picture, V_O centres are responsible for a sharp transition at ≈ 2.7 eV, appreciable both in absorption and fluorescence spectra of all samples. The trend in the fluorescence emission of this transition mirrors, however, neither that in light absorption nor in the V_O content based on local structural data. A possible explanation invokes the O_2 -induced quenching of fluorescence. It is well known that, under the action of UV light, polycrystalline TiO_2 can promote the formation of highly reactive oxygen species (ROS), like superoxide radicals (O_2^-)⁶⁵ or singlet dioxygen (1O_2).^{66,67} Experimental evidence^{65,66,68} suggests that ROS formation involves an initial absorption of ground-state triplet O_2 at surface V_O 's, followed by an electron transfer from vacancy-related Ti^{3+} species.⁶⁹ The quenching of the characteristic emission of V_O 's is likely a byproduct of the UV-induced interaction of surface vacancies with O_2 . We hypothesize that the strong I_D reduction in TNT samples be ascribable to stronger O_2 -induced quenching, which in turn is expected to depend on a higher concentration of surface V_O 's. The combination of EXAFS and CM outcomes thus indicate that TNT materials have the greatest amount of surface V_O 's compared to the pristine reference (Figure 6). Conversely, V_O 's are mainly of bulk nature in TNU, that is, they are buried deep inside the nanoparticles, being preserved from interaction with O_2 . In this respect, it should be noted that TNU samples have lower surface area and porosity than the TNN and TNT series (Table 1). The TNN series exhibits an intermediate behaviour, with TNN0.1 showing a similar fluorescence emission than T, and TNN0.5 displaying a reduced PL emission, possibly related to the sample's higher crystallinity and promoted UV-light photocatalytic activity. This scenario awaits experimental confirmation through dedicated measurements in controlled oxidant environments. It is worth noting, however, that an analogue conclusion was drawn for O-defective CeO_2 nanoparticles, which were proposed to exploit quenching of fluorescence for applications in oxygen detection.⁷⁰

These diverse landscapes in terms of intrinsic and extrinsic defects give rise to notably different photochromic and photocatalytic properties. Transient absorption features have been related to trap states, hence have been used to investigate the defectivity of TiO_2 .¹¹ Here, the photochromic peak at the highest energy falls at ca. 3.0 eV for the TNN and TNU series and < 3 eV for TNT samples, *i.e.* ca. 0.2 eV below the band gap value of each sample. Electron trapping states located ca. 0.26 eV below the CB edge have been previously related to Ti^{3+} ions.^{11,71} Mendoza Diaz et al. recently studied the PL emission of TiO_2 samples using scavengers: a PL peak at ca. 2.9 eV was attributed to recombination between electrons trapped in shallow trapping states due to Ti^{3+} species associated with Ti interstitials, and holes in the VB.²⁶ With respect to PL transitions, here the transient absorption features are produced by UV irradiation over the course of minutes and are stable for several hours. Indeed, slow interconversions between electron traps, taking place over the course of minutes to hours at 0–50 °C, have been previously reported in reduced TiO_2 systems and attributed to equilibration in

trap states involving changes in structure or stoichiometry.⁷² Also the absorption feature centered between 2.2 and 2.3 eV has been previously reported and assigned to the 2T_2 to 2E transition of Ti^{3+} .^{73,74} Furthermore, Serpone and coauthors consistently reported a photochromic peak at 2.16 eV upon UV light irradiation of N-doped TiO_2 samples, which was attributed to Ti^{3+} centres^{54,75}. The TNN and TNU photochromic features, as well as some of the TNT ones, could thus be related to photogenerated Ti^{3+} species. These features are observed only in the N-modified samples, suggesting that the addition of these external sources, particularly ammonia and urea, introduce electron donor species, which, in turn, lead to the formation of Ti^{3+} species upon light irradiation.⁷⁶

Furthermore, the TNT0.5 sample shows a marked photochromic component at ca. 1.5 eV: this observation, along with the increased V_O content and low PL emission of this sample, suggests that this component could be related to Ti^{3+} species associated with surface V_O . Notably, Kuznetsov and coauthors⁵⁶ attributed a photochromic peak at 1.56 eV to extra-charged Ti^{3+} species ($Ti^{\delta+}$), such as two adjacent Ti^{3+} centers located near a single oxygen vacancy, whose formation occurs only at high density of photogenerated Ti^{3+} centers.

Hence, the photochromic behaviour of all N modified samples highlights the occurrence of trap states for photogenerated electrons due to lattice defects formed upon N addition during synthesis. Overall, the presence of trap sites in N-modified samples goes hand in hand with poorer photocatalytic performance under UV irradiation. The only notable exception is TNN0.5: This sample is characterized by larger crystallites and higher anatase content, which have been related to reduced recombination of photogenerated charges (see confocal microscopy results) and promoted photocatalytic activity.

Visible-light tests also show mixed results. The visible-absorbing species in TNU and TNN fail to promote visible-light activity, which could be related to an insufficient oxidation potential or mobility of trapped holes to generate highly oxidizing radicals.^{28,77} Conversely, the TNT series displays visible light activity, which could be due to its N substitutional doping. In the TNT series, the highest activity is achieved by TNT0.1. Notably, TNT0.1 is the only sample displaying some detrapping effects upon light irradiation. It is widely accepted that charge transfer occurs from Ti^{3+} states to singly occupied N-states:⁷⁸



Moreover, light irradiation regenerates paramagnetic N_b^{\bullet} centers from N_b^- states by exciting electrons to the conduction band, which are then captured by adsorbed O_2 .⁷⁸ Hence, the presence of substitutional nitrogen could promote detrapping of Ti^{3+} -related states. However, if V_O 's are in excess compared to N states, the Ti^{3+} states still remain partially populated.²⁰ This could explain why the V_O -rich TNT0.5 sample displays such a different photochromic behavior compared to TNT0.1. The

presence of trap sites related to extra-charged Ti^{3+} could, in turn, rationalize the lower visible-light activity of TNT0.5 compared to TNT0.1.

5. CONCLUSIONS

In this work, we applied a multidisciplinary approach, including advanced spectroscopy and microscopy methods, to investigate the role of oxygen vacancies (V_{O} 's) in highly defective nanostructured TiO_2 matrices. Plane wave bulk quantum simulations complemented the experimental picture. The purpose was twofold: on the one hand, to explore the distribution and role of surface and bulk V_{O} 's; on the other hand, to study how V_{O} 's may affect the photophysical and photochemical properties of TiO_2 . The amount of V_{O} species was tuned by addition of an extrinsic defect, nitrogen. As a matter of fact, thermodynamics ensures that the concentration of bulk N and extra V_{O} 's are correlated, despite being both not easily amenable to quantitative experimental determination.

UV-vis fluorescence showed a characteristic spectral signal in the blue range of the visible window (≈ 2.7 eV, 461-464 nm), which was present already in the pristine TiO_2 reference. High-grade DFT simulations demonstrated that this signature is specific of V_{O} defects. Excess electrons coming from a V_{O} are highly localized on at least two reduced Ti ions around the vacancy. In turn, this produces sharp mid-gap states, which are involved in rapid excitation-recombination processes with almost no Stokes shift.

Further insights into the quantity and distribution of V_{O} 's within the nanostructured particles were obtained by comparing local structural information, gained by a combination of EXAFS and DFT data, with fluorescence density output per μm^2 , measured by confocal microscopy. We hypothesize that, in the case of the TNT series, the V_{O} excess does not promote fluorescence emission due to the surface nature of these defects, which can interact with adsorbed oxygen species under UV pumping. We propose that confocal microscopy might be employed as a cheap tool to discriminate the distribution of V_{O} 's in nanostructured TiO_2 : the more effective the fluorescence quenching, the higher the amount of surface V_{O} 's.

Actually, a lowered fluorescence in N-modified species is correlated with a promoted photocatalytic activity, as TNN0.5 and the TNT series are the best performing samples under UV and visible sources, respectively. The photocatalytic features of the latter samples could be attributed to substitutional N doping, as other N-related defects, such as those prevalent in the TNU and TNN series, are not visible-active despite absorbing visible-light.

The intrinsic defects play a notable role as well in the photochromic and photocatalytic properties of the N-modified samples. A good balance between the extrinsic and intrinsic defects, such as in TNT0.1, seems related to detrapping phenomena and an ensuing enhanced photocatalytic

activity in the visible region. A further increase in V_O content (even surface ones) could promote the formation of other electron traps, such as photo-induced extra-charged Ti^{3+} species, slightly worsening the photocatalytic performance.

ASSOCIATED CONTENT

Supporting Information

The Supporting Information is available free of charge at <https://pubs.acs.org/doi/10.1021/acs.jpcc.xxxxxx>. EXAFS results. Details of bulk DFT simulations. Confocal microscopy results. Photochromism. Photocatalysis.

AUTHOR INFORMATION

Corresponding Author

Leonardo Lo Presti – *Università degli Studi di Milano, Dipartimento di Chimica, Via Golgi 19, 20133 Milano (Italy) and Istituto Nazionale di Fisica Nucleare (INFN), Laboratori Nazionali di Frascati, Frascati (Italy)*
orcid.org/0000-0001-6361-477X Email: leonardo.lopresti@unimi.it

Authors

Daniela Meroni – *Università degli Studi di Milano, Dipartimento di Chimica, Via Golgi 19, 20133 Milano (Italy); Consorzio INSTM, via Giusti 9, 50121 Florence (Italy)*

Carolina Cionti – *Università degli Studi di Milano, Dipartimento di Chimica, Via Golgi 19, 20133 Milano (Italy)*

Lucia Silvestrini – *Institute of Microbial Genetics, Department of Applied Genetics and Cell Biology, University of Natural Resources and Life Sciences (BOKU), Konrad Lorenz Straße 24, 3430 Tulln an der Donau (Austria)*

Noga Gal – *Department of Bionosciences, University of Natural Resources and Life Sciences (BOKU), Muthgasse 11/II, 1190 Vienna (Austria)*

Marco Cazzaniga – *Università degli Studi di Milano, Dipartimento di Chimica, Via Golgi 19, 20133 Milano (Italy)*

Michele Ceotto – *Università degli Studi di Milano, Dipartimento di Chimica, Via Golgi 19, 20133 Milano (Italy)*

Giacomo Buccella – *Politecnico di Milano, Department of Chemistry, Materials and Chemical Engineering "Giulio Natta", Piazza Leonardo da Vinci 32, Milano (Italy)*

Giuseppe Cappelletti – *Università degli Studi di Milano, Dipartimento di Chimica, Via Golgi 19, 20133 Milano (Italy); Consorzio INSTM, via Giusti 9, 50121 Florence (Italy)*

Complete contact information is available at: <https://pubs.acs.org/doi/10.1021/acs.jpcc.xxxxxx>

Notes

The authors declare no competing financial interest.

References

- (1) Gusain, R.; Gupta, K.; Joshi, P.; Khatri, O. P. Adsorptive Removal and Photocatalytic Degradation of Organic Pollutants Using Metal Oxides and Their Composites: A Comprehensive Review. *Adv. Colloid Interface Sci.* **2019**, *272*, 102009.
- (2) Shi, J.; Zhang, J.; Yang, L.; Qu, M.; Qi, D.; Zhang, K. H. L. Wide Bandgap Oxide Semiconductors: From Materials Physics to Optoelectronic Devices. *Adv. Mater.* **2021**, *33* (50), 2006230.
- (3) Ji, H.; Zeng, W.; Li, Y. Gas Sensing Mechanisms of Metal Oxide Semiconductors: A Focus Review. *Nanoscale* **2019**, *11* (47), 22664–22684.
- (4) Zhang, T.; He, Q.; Yu, J.; Chen, A.; Zhang, Z.; Pan, J. Recent Progress in Improving Strategies of Inorganic Electron Transport Layers for Perovskite Solar Cells. *Nano Energy* **2022**, *104*, 107918.
- (5) Liu, J.; Luo, Z.; Mao, X.; Dong, Y.; Peng, L.; Sun-Waterhouse, D.; Kennedy, J. V.; Waterhouse, G. I. N.; Liu, J.; Luo, Z.; et al. Recent Advances in Self-Supported Semiconductor Heterojunction Nanoarrays as Efficient Photoanodes for Photoelectrochemical Water Splitting. *Small* **2022**, *18* (48), 2204553.
- (6) Putri, L. K.; Ng, B. J.; Ong, W. J.; Chai, S. P.; Mohamed, A. R. Toward Excellence in Photocathode Engineering for Photoelectrochemical CO₂ Reduction: Design Rationales and Current Progress. *Adv. Energy Mater.* **2022**, *12* (41), 2201093.
- (7) Lo Presti, L.; Ceotto, M.; Spadavecchia, F.; Cappelletti, G.; Meroni, D.; Acres, R. G.; Ardizzone, S. Role of the Nitrogen Source in Determining Structure and Morphology of N-Doped Nanocrystalline TiO₂. *J. Phys. Chem. C* **2014**, *118* (9), 4797–4807.
- (8) Spadavecchia, F.; Cappelletti, G.; Ardizzone, S.; Ceotto, M.; Azzola, M. S.; Lo Presti, L.; Cerrato, G.; Falciola, L. Role of Pr on the Semiconductor Properties of Nanotitania. An Experimental and First-Principles Investigation. *J. Phys. Chem. C* **2012**, *116* (43), 23083–23093.
- (9) Marchiori, C.; Di Liberto, G.; Soliveri, G.; Loconte, L.; Lo Presti, L.; Meroni, D.; Ceotto, M.; Oliva, C.; Cappelli, S.; Cappelletti, G.; et al. Unraveling the Cooperative Mechanism of Visible-Light Absorption in Bulk N,Nb Codoped TiO₂ Powders of Nanomaterials. *J. Phys. Chem. C* **2015**, *118* (41), 24152–24164.
- (10) Rimoldi, L.; Ambrosi, C.; Di Liberto, G.; Lo Presti, L.; Ceotto, M.; Oliva, C.; Meroni, D.; Cappelli, S.; Cappelletti, G.; Soliveri, G.; et al. Impregnation versus Bulk Synthesis: How the Synthetic Route Affects the Photocatalytic Efficiency of Nb/Ta:N Codoped TiO₂ Nanomaterials. *J. Phys. Chem. C* **2015**, *119* (42), 24104–24115.

- (11) Liu, B.; Zhao, X.; Yu, J.; Parkin, I. P.; Fujishima, A.; Nakata, K. Intrinsic Intermediate Gap States of TiO₂ Materials and Their Roles in Charge Carrier Kinetics. *J. Photochem. Photobiol. C Photochem. Rev.* **2019**, *39*, 1–57.
- (12) Bai, S.; Zhang, N.; Gao, C.; Xiong, Y. Defect Engineering in Photocatalytic Materials. *Nano Energy* **2018**, *53*, 296–336.
- (13) Nowotny, J.; Alim, M. A.; Bak, T.; Idris, M. A.; Ionescu, M.; Prince, K.; Sahdan, M. Z.; Sopian, K.; Mat Teridi, M. A.; Sigmund, W. Defect Chemistry and Defect Engineering of TiO₂-Based Semiconductors for Solar Energy Conversion. *Chem. Soc. Rev.* **2015**, *44* (23), 8424–8442.
- (14) Hou, L.; Guan, Z.; Zhang, M.; He, C.; Li, Q.; Yang, J. Adjusting the Ratio of Bulk Single-Electron-Trapped Oxygen Vacancies/Surface Oxygen Vacancies in TiO₂ for Efficient Photocatalytic Hydrogen Evolution. *Catal. Sci. Technol.* **2018**, *8* (11), 2809–2817.
- (15) Yu, X.; Kim, B.; Kim, Y. K. Highly Enhanced Photoactivity of Anatase TiO₂ Nanocrystals by Controlled Hydrogenation-Induced Surface Defects. *ACS Catal.* **2013**, *3* (11), 2479–2486.
- (16) Sun, Q.; Cortie, D.; Zhang, S.; Frankcombe, T. J.; She, G.; Gao, J.; Sheppard, L. R.; Hu, W.; Chen, H.; Zhuo, S.; et al. The Formation of Defect-Pairs for Highly Efficient Visible-Light Catalysts. *Adv. Mater.* **2017**, *29* (11), 3601.
- (17) Wu, Q.; Zheng, Q.; Van De Krol, R. Creating Oxygen Vacancies as a Novel Strategy to Form Tetrahedrally Coordinated Ti⁴⁺ in Fe/TiO₂ Nanoparticles. *J. Phys. Chem. C* **2012**, *116* (12), 7219–7226.
- (18) Ariyanti, D.; Mills, L.; Dong, J.; Yao, Y.; Gao, W. NaBH₄ Modified TiO₂: Defect Site Enhancement Related to Its Photocatalytic Activity. *Mater. Chem. Phys.* **2017**, *199*, 571–576.
- (19) Di Valentin, C.; Pacchioni, G.; Selloni, A. Reduced and N-Type Doped TiO₂: Nature of Ti³⁺ Species. *J. Phys. Chem. C* **2009**, *113* (48), 20543–20552.
- (20) Spadavecchia, F.; Cappelletti, G.; Ardizzone, S.; Ceotto, M.; Falciola, L. Electronic Structure of Pure and N-Doped TiO₂ Nanocrystals by Electrochemical Experiments and First Principles Calculations. *J. Phys. Chem. C* **2011**, *115* (14), 6381–6391.
- (21) chu, B.; Ou, X.; Wei, L.; Liu, H.; chen, K.; Qin, Q.; Meng, L.; Fan, M.; Li, B.; Dong, L. Insight into the Effect of Oxygen Vacancies and OH Groups on Anatase TiO₂ for CO Oxidation: A Combined FT-IR and Density Functional Theory Study. *Mol. Catal.* **2021**, *511*, 111755.
- (22) Sun, Q.; Cortie, D.; Zhang, S.; Frankcombe, T. J.; She, G.; Gao, J.; Sheppard, L. R.; Hu, W.; Chen, H.; Zhuo, S.; et al. The Formation of Defect-Pairs for Highly Efficient Visible-Light

- Catalysts. *Adv. Mater.* **2017**, *29* (11), 1–6.
- (23) Li, G.; Huang, R.; Zhu, C.; Jia, G.; Zhang, S.; Zhong, Q. Effect of Oxygen Vacancies and Its Quantity on Photocatalytic Oxidation Performance of Titanium Dioxide for NO Removal. *Colloids Surfaces A Physicochem. Eng. Asp.* **2021**, *614*, 126156.
- (24) Cao, T.; Xia, T.; Zhou, L.; Li, G.; Chen, X.; Tian, H.; Zhao, J.; Wang, J. O.; Zhang, W.; Li, S.; et al. Distribution and Concentration of Surface Oxygen Vacancy of TiO₂ and Its Photocatalytic Activity. *J. Phys. D. Appl. Phys.* **2020**, *53* (42), 424001.
- (25) Huang, J.; Dou, L.; Li, J.; Zhong, J.; Li, M.; Wang, T. Excellent Visible Light Responsive Photocatalytic Behavior of N-Doped TiO₂ toward Decontamination of Organic Pollutants. *J. Hazard. Mater.* **2021**, *403*, 123857.
- (26) Mendoza Diaz, M. I.; Balocchi, A.; Oyekan, K.; Tan, K.; Vandenberghe, W. G.; Esteve, A.; Rossi, C. Dominant Role of OH⁻ and Ti³⁺ Defects on the Electronic Structure of TiO₂ Thin Films for Water Splitting. *Dalt. Trans.* **2022**, *51* (40), 15300–15311.
- (27) Ceotto, M.; Lo Presti, L.; Cappelletti, G.; Meroni, D.; Spadavecchia, F.; Zecca, R.; Leoni, M.; Scardi, P.; Bianchi, C. L.; Ardizzone, S. About the Nitrogen Location in Nanocrystalline N-Doped TiO₂: Combined DFT and EXAFS Approach. *J. Phys. Chem. C* **2012**, *116* (2), 1764–1771.
- (28) Rengifo-Herrera, J. A.; Osorio-Vargas, P.; Pulgarin, C. A Critical Review on N-Modified TiO₂ Limits to Treat Chemical and Biological Contaminants in Water. Evidence That Enhanced Visible Light Absorption Does Not Lead to Higher Degradation Rates under Whole Solar Light. *J. Hazard. Mater.* **2022**, *425*, 127979.
- (29) Mitoraj, D.; Kisch, H. The Nature of Nitrogen-Modified Titanium Dioxide Photocatalysts Active in Visible Light. *Angew. Chemie Int. Ed.* **2008**, *47* (51), 9975–9978.
- (30) Rimoldi, L.; Giordana, A.; Cerrato, G.; Falletta, E.; Meroni, D. Insights on the Photocatalytic Degradation Processes Supported by TiO₂/WO₃ Systems. The Case of Ethanol and Tetracycline. *Catal. Today* **2019**, *328*, 210–215.
- (31) Ravel, B.; Newville, M. ATHENA, ARTEMIS, HEPHAESTUS: Data Analysis for X-Ray Absorption Spectroscopy Using IFEFFIT. *urn:issn:0909-0495* **2005**, *12* (4), 537–541.
- (32) Newville, M. IFEFFIT: Interactive XAFS Analysis and FEFF Fitting. *J. Synchrotron Radiat.* **2001**, *8* (2), 322–324.
- (33) Angulo, G.; Grampp, G.; Rosspeintner, A. Recalling the Appropriate Representation of Electronic Spectra. *Spectrochim. Acta Part A Mol. Biomol. Spectrosc.* **2006**, *65* (3–4), 727–731.
- (34) Schindelin, J.; Arganda-Carreras, I.; Frise, E.; Kaynig, V.; Longair, M.; Pietzsch, T.;

- Preibisch, S.; Rueden, C.; Saalfeld, S.; Schmid, B.; et al. Fiji: An Open-Source Platform for Biological-Image Analysis. *Nat. Methods* 2012 97 **2012**, 9 (7), 676–682.
- (35) Soliveri, G.; Ardizzone, S.; Antonello, A.; Meroni, D.; Cappelletti, G. Photocatalytic Remediation of Indoor Pollution by Transparent TiO₂ Films. *Catal. Today* **2014**, 230, 35–40.
- (36) Giannozzi, P.; Andreussi, O.; Brumme, T.; Bunau, O.; Buongiorno Nardelli, M.; Calandra, M.; Car, R.; Cavazzoni, C.; Ceresoli, D.; Cococcioni, M.; et al. Advanced Capabilities for Materials Modelling with Quantum ESPRESSO. *J. Phys. Condens. Matter* **2017**, 29 (46), 465901.
- (37) Giannozzi, P.; Baroni, S.; Bonini, N.; Calandra, M.; Car, R.; Cavazzoni, C.; Ceresoli, D.; Chiarotti, G. L.; Cococcioni, M.; Dabo, I.; et al. QUANTUM ESPRESSO: A Modular and Open-Source Software Project for Quantum of Materials. *J. Phys. Condens. Matter* **2009**, 21 (39), 395502.
- (38) Giannozzi, P.; Baseggio, O.; Bonfà, P.; Brunato, D.; Car, R.; Carnimeo, I.; Cavazzoni, C.; De Gironcoli, S.; Delugas, P.; Ferrari Ruffino, F.; et al. Quantum ESPRESSO toward the Exascale. *J. Chem. Phys.* **2020**, 152 (15), 154105.
- (39) Hu, Z.; Metiu, H. Choice of U for DFT+ U Calculations for Titanium Oxides. *J. Phys. Chem. C* **2011**, 115 (13), 5841–5845.
- (40) Arroyo-De Dompablo, M. E.; Morales-Garca, A.; Taravillo, M. DFT+U Calculations of Crystal Lattice, Electronic Structure, and Phase Stability under Pressure of TiO₂ Polymorphs. *J. Chem. Phys.* **2011**, 135 (5), 054503.
- (41) Diebold, U. The Surface Science of Titanium Dioxide. *Surf. Sci. Rep.* **2003**, 48 (5–8), 53–229.
- (42) Mattioli, G.; Filippone, F.; Alippi, P.; Amore Bonapasta, A. Ab Initio Study of the Electronic States Induced by Oxygen Vacancies in Rutile and Anatase TiO₂. *Phys. Rev. B - Condens. Matter Mater. Phys.* **2008**, 78 (24), 3–6.
- (43) Finazzi, E.; Di Valentin, C.; Pacchioni, G.; Selloni, A. Excess Electron States in Reduced Bulk Anatase TiO₂: Comparison of Standard GGA, GGA+U, and Hybrid DFT Calculations. *J. Chem. Phys.* **2008**, 129 (15), 154113.
- (44) Morgan, B. J.; Watson, G. W. Intrinsic N-Type Defect Formation in TiO₂: A Comparison of Rutile and Anatase from GGA+U Calculations. *J. Phys. Chem. C* **2010**, 114 (5), 2321–2328.
- (45) Yang, K.; Dai, Y.; Huang, B.; Feng, Y. P. Density-Functional Characterization of Antiferromagnetism in Oxygen-Deficient Anatase and Rutile TiO₂. *Phys. Rev. B - Condens. Matter Mater. Phys.* **2010**, 81 (3), 033202.
- (46) Yamamoto, T.; Ohno, T. A Hybrid Density Functional Study on the Electron and Hole Trap

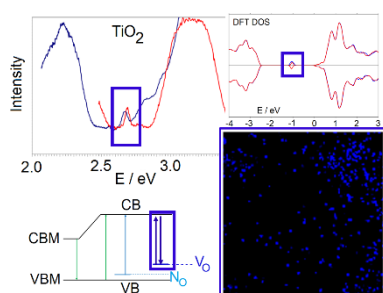
- States in Anatase Titanium Dioxide. *Phys. Chem. Chem. Phys.* **2011**, *14* (2), 589–598.
- (47) Raghav, A.; Tri Hanindriyo, A.; Utimula, K.; Abbasnejad, M.; Maezono, R.; Panda, E. Intrinsic Electronic Defect States of Anatase Using Density Functional Theory. *Comput. Mater. Sci.* **2020**, *184*, 109925.
- (48) Otero-de-la-Roza, A.; Blanco, M. A.; Pendás, A. M.; Luaña, V. Critic: A New Program for the Topological Analysis of Solid-State Electron Densities. *Comput. Phys. Commun.* **2009**, *180* (1), 157–166.
- (49) Otero-De-La-Roza, A.; Johnson, E. R.; Luaña, V. Critic2: A Program for Real-Space Analysis of Quantum Chemical Interactions in Solids. *Comput. Phys. Commun.* **2014**, *185* (3), 1007–1018.
- (50) Meroni, D.; Ardizzone, S.; Cappelletti, G.; Oliva, C.; Ceotto, M.; Poelman, D.; Poelman, H. Photocatalytic Removal of Ethanol and Acetaldehyde by N-Promoted TiO₂ Films: The Role of the Different Nitrogen Sources. *Catal. Today* **2011**, *161* (1), 169–174.
- (51) Boonprakob, N.; Wetchakun, N.; Phanichphant, S.; Waxler, D.; Sherrell, P.; Nattestad, A.; Chen, J.; Inceesungvorn, B. Enhanced Visible-Light Photocatalytic Activity of g-C₃N₄/TiO₂ Films. *J. Colloid Interface Sci.* **2014**, *417*, 402–409.
- (52) Ceotto, M.; Lo Presti, L.; Cappelletti, G.; Meroni, D.; Spadavecchia, F.; Zecca, R.; Leoni, M.; Scardi, P.; Bianchi, C. L.; Ardizzone, S. About the Nitrogen Location in Nanocrystalline N-Doped TiO₂: Combined DFT and EXAFS Approach. *J. Phys. Chem. C* **2012**, *116* (2), 1764–1771.
- (53) Howard, C J, Sabine, T M, Dickson, F. Structural and Thermal Parameters for Rutile and Anatase. *Acta Crystallogr. B* **1991**, *47* ((39,1983-)), 462–468.
- (54) Kuznetsov, V. N.; Glazkova, N. I.; Mikhaylov, R. V.; Serpone, N. In Situ Study of Photo- and Thermo-Induced Color Centers in Photochromic Rutile TiO₂ in the Temperature Range 90–720 K. *Photochem. Photobiol. Sci.* **2016**, *15* (10), 1289–1298.
- (55) Kuznetsov, V. N.; Glazkova, N. I.; Mikhaylov, R. V.; Serpone, N. Additional Specific Channel of Photoactivation of Solid Semiconductors. A Revisit of the Thermo-/Photo-Stimulated Bleaching of Photoinduced Ti³⁺ Color Centers in Visible-Light-Active Photochromic Rutile Titania. *J. Phys. Chem. C* **2018**, *122* (25), 13294–13303.
- (56) Kuznetsov, V. N.; Glazkova, N. I.; Mikhaylov, R. V.; Kozhevina, A. V.; Serpone, N. Photophysics of Color Centers in Visible-Light-Active Rutile Titania. Evidence of the Photoformation and Trapping of Charge Carriers from Advanced Diffuse Reflectance Spectroscopy and Mass Spectrometry. *Catal. Today* **2020**, *340*, 58–69.
- (57) Bader, R. F. W. *Atoms in Molecules. A Quantum Theory*, 1st ed.; Oxford : Clarendon Press,

Ed.; Oxford University Press: Oxford U.K., 1995.

- (58) Lo Presti, L.; Pifferi, V.; Di Liberto, G.; Cappelletti, G.; Falciola, L.; Cerrato, G.; Ceotto, M. Direct Measurement and Modeling of Spontaneous Charge Migration across Anatase–Brookite Nanoheterojunctions. *J. Mater. Chem. A* **2021**, *9* (12), 7782–7790.
- (59) Di Liberto, G.; Pifferi, V.; Lo Presti, L.; Ceotto, M.; Falciola, L. Atomistic Explanation for Interlayer Charge Transfer in Metal-Semiconductor Nanocomposites: The Case of Silver and Anatase. *J. Phys. Chem. Lett.* **2017**, *8* (21), 5372–5377.
- (60) Lei, Y.; Zhang, L. D.; Meng, G. W.; Li, G. H.; Zhang, X. Y.; Liang, C. H.; Chen, W.; Wang, S. X. Preparation and Photoluminescence of Highly Ordered TiO₂ Nanowire Arrays. *Appl. Phys. Lett.* **2001**, *78* (8), 1125.
- (61) Paddock, S. W. *Confocal Microscopy. Methods and Protocols*, 2nd ed.; Paddock, S. W., Ed.; Methods in Molecular Biology; Springer New York: New York, NY, 2014; Vol. 1075.
- (62) Pargoletti, E.; Rimoldi, L.; Meroni, D.; Cappelletti, G. Photocatalytic Removal of Gaseous Ethanol, Acetaldehyde and Acetic Acid: From a Fundamental Approach to Real Cases. <https://doi.org/10.1080/09506608.2021.2017390> **2022**, *67* (8), 864–897.
- (63) Tang, J.; Cowan, A. J.; Durrant, J. R.; Klug, D. R. Mechanism of O₂ Production from Water Splitting: Nature of Charge Carriers in Nitrogen Doped Nanocrystalline TiO₂ Films and Factors Limiting O₂ Production. *J. Phys. Chem. C* **2011**, *115* (7), 3143–3150.
- (64) Di Valentin, C.; Pacchioni, G.; Selloni, A.; Livraghi, S.; Giamello, E. Characterization of Paramagnetic Species in N-Doped TiO₂ Powders by EPR Spectroscopy and DFT Calculations. *J. Phys. Chem. B* **2005**, *109* (23), 11414–11419.
- (65) Carter, E.; Carley, A. F.; Murphy, D. M. Evidence for O₂- Radical Stabilization at Surface Oxygen Vacancies on Polycrystalline TiO₂. *J. Phys. Chem. C* **2007**, *111* (28), 10630–10638.
- (66) Jańczyk, A.; Krakowska, E.; Stochel, G.; Macyk, W. Singlet Oxygen Photogeneration at Surface Modified Titanium Dioxide. *J. Am. Chem. Soc.* **2006**, *128* (49), 15574–15575.
- (67) Chiesa, M.; Livraghi, S.; Paganini, M. C.; Salvadori, E.; Giamello, E. Nitrogen-Doped Semiconducting Oxides. Implications on Photochemical, Photocatalytic and Electronic Properties Derived from EPR Spectroscopy. *Chem. Sci.* **2020**, *11* (26), 6623–6641.
- (68) Hurum, D. C.; Agrios, A. G.; Gray, K. A.; Rajh, T.; Thurnauer, M. C. Explaining the Enhanced Photocatalytic Activity of Degussa P25 Mixed-Phase TiO₂ Using EPR. *J. Phys. Chem. B* **2003**, *107* (19), 4545–4549.
- (69) Murata, C.; Yoshida, H.; Kumagai, J.; Hattori, T. Active Sites and Active Oxygen Species for Photocatalytic Epoxidation of Propene by Molecular Oxygen over TiO₂-SiO₂ Binary Oxides. *J. Phys. Chem. B* **2003**, *107* (18), 4364–4373.

- (70) Shehata, N.; Meehan, K.; Leber, D. E. Fluorescence Quenching in Ceria Nanoparticles: Dissolved Oxygen Molecular Probe with Relatively Temperature Insensitive Stern-Volmer Constant up to 50°C. *https://doi.org/10.1117/1.JNP.6.063529* **2012**, *6* (1), 063529.
- (71) Reckers, P.; Dimamay, M.; Klett, J.; Trost, S.; Zilberberg, K.; Riedl, T.; Parkinson, B. A.; Brötz, J.; Jaegermann, W.; Mayer, T. Deep and Shallow TiO₂ Gap States on Cleaved Anatase Single Crystal (101) Surfaces, Nanocrystalline Anatase Films, and ALD Titania Ante and Post Annealing. *J. Phys. Chem. C* **2015**, *119* (18), 9890–9898.
- (72) Peper, J. L.; Vinyard, D. J.; Brudvig, G. W.; Mayer, J. M. Slow Equilibration between Spectroscopically Distinct Trap States in Reduced TiO₂ Nanoparticles. *J. Am. Chem. Soc.* **2017**, *139* (8), 2868–2871.
- (73) Sekiya, T.; Ichimura, K.; Igarashi, M.; Kurita, S. Absorption Spectra of Anatase TiO₂ Single Crystals Heat-Treated under Oxygen Atmosphere. *J. Phys. Chem. Solids* **2000**, *61* (8), 1237–1242.
- (74) Choudhury, B.; Choudhury, A. Oxygen Defect Dependent Variation of Band Gap, Urbach Energy and Luminescence Property of Anatase, Anatase–Rutile Mixed Phase and of Rutile Phases of TiO₂ Nanoparticles. *Phys. E Low-dimensional Syst. Nanostructures* **2014**, *56*, 364–371.
- (75) Kuznetsov, V. N.; Emeline, A. V.; Glazkova, N. I.; Mikhaylov, R. V.; Serpone, N. Real-Time in Situ Monitoring of Optical Absorption Changes in Visible-Light-Active TiO₂ under Light Irradiation and Temperature-Programmed Annealing. *J. Phys. Chem. C* **2014**, *118* (47), 27583–27593.
- (76) Freitag, J.; Domínguez, A.; Niehaus, T. A.; Hülsewig, A.; Dillert, R.; Frauenheim, T.; Bahnemann, D. W. Nitrogen(II) Oxide Charge Transfer Complexes on TiO₂: A New Source for Visible-Light Activity. *J. Phys. Chem. C* **2015**, *119* (9), 4488–4501.
- (77) Hirakawa, T.; Nosaka, Y. Selective Production of Superoxide Ions and Hydrogen Peroxide over Nitrogen- and Sulfur-Doped TiO₂ Photocatalysts with Visible Light in Aqueous Suspension Systems. *J. Phys. Chem. C* **2008**, *112* (40), 15818–15823.
- (78) Livraghi, S.; Paganini, M. C.; Giamello, E.; Selloni, A.; Di Valentin, C.; Pacchioni, G. Origin of Photoactivity of Nitrogen-Doped Titanium Dioxide under Visible Light. *J. Am. Chem. Soc.* **2006**, *128* (49), 15666–15671.

For Table of Content Graphics Use Only



Synergy of visible light probes and DFT calculations allow to highlight the preferential location and the relative content of oxygen vacancies in highly defective TiO₂ materials